Rotation Period Detection for Earth-like Exoplanets

Jiazheng Li[1] , Jonathan H. Jiang[2] , Huanzhou Yang[3] , Dorian S. Abbot[3] , Renyu Hu[2] , Thaddeus D. Komacek[3] ,
Stuart J. Bartlett[1] , and Yuk L. Yung[1,2]
[1] Division of Geological and Planetary Science, California Institute of Technology, Pasadena, CA, USA; jiazheng@caltech.edu
[2] Jet Propulsion Laboratory, California Institute of Technology, Pasadena, CA, USA
[3] Department of the Geophysical Sciences, The University of Chicago, Chicago, IL, USA

Abstract

A terrestrial planet's rotation period is one of the key parameters that determines its climate and habitability. Current methods for detecting the rotation period of exoplanets are not suitable for terrestrial exoplanets. Here we demonstrate that, under certain conditions, the rotation period of an Earth-like exoplanet will be detectable using direct-imaging techniques. We use a global climate model that includes clouds to simulate reflected starlight from an Earth-like exoplanet and explore how different parameters (e.g., orbital geometry, wavelength, time resolution) influence the detectability of the planet's rotation period. We show that the rotation period of an Earth-like exoplanet is detectable using visible-wavelength channels with time-series monitoring at a signal-to-noise ratio (S/N) >20 with ∼5–15 rotation periods of data, while the rotation period of a planet with full ocean coverage is unlikely to be detectable. To better detect the rotation period, one needs to plan the observation so that each individual integration would yield a S/N >10, while keeping the integration time shorter than $1/6$ to $1/4$ of the rotation period of the planet. Our results provide important guidance for rotation period detection of Earth-like exoplanets in reflected light using future space telescopes.

Unified Astronomy Thesaurus concepts: Exoplanets (498); Exoplanet detection methods (489); Direct imaging (387)

1. Introduction

Since the rotation rate of a planet determines the magnitude of its Coriolis force, and therefore strongly influences its atmospheric and oceanic circulation, it is one of the key parameters that determines the climate of a planet (Showman et al. 2013; Forget & Leconte 2014; Kaspi & Showman 2015; Komacek & Abbot 2019). Moreover, as a result of cloud feedbacks, previous simulations suggest that a slowly rotating Earth-like planet could maintain a habitable climate at nearly twice the incident stellar flux as Earth, which implies a strong dependence of the inner edge of the habitable zone on planetary rotation rate (Yang et al. 2014; Way et al. 2016). Therefore, detecting the rotation period of an exoplanet is crucial for evaluating its habitability. Furthermore, the rotation period of an exoplanet will evolve toward the orbital period due to tidal forces exerted by the star it orbits, especially for potentially habitable exoplanets in close-in orbits around low-mass stars (Kasting et al. 1993). Barnes (2017) calculated that approximately half of the habitable Kepler planets and most of the habitable Transiting Exoplanet Survey Satellite planets should be tidally locked within 1 Gyr. Detecting the rotation period of an exoplanet, and determining whether it is tidally locked, will therefore put constraints on the age of an exoplanetary system.

A number of methods are currently being used to detect the rotation period of exoplanets. The first method is to use the rotational broadening and Doppler shift of lines in the planetary atmosphere to determine the rotational velocity of the exoplanet. For example, Snellen et al. (2014) used the CO spectrum to constrain the rotational velocity of the gas giant β Pictoris b and Brogi et al. (2016) used the CO and H_2O spectra to constrain the rotational velocity of HD 189733b. The second method is to

infer the rotation period of an exoplanet from the magnetic-field-induced radio emission from the extrasolar system. For example, Hess & Zarka (2011) modeled the dynamic radio spectra from an exoplanet and its parent star to show that physical information about the system, including the magnetic field and the rotation period of the exoplanet, can be obtained from radio observations.

These two methods are optimal for hot Jupiters and directly imaged wide-separation gas giants, which are likely to have high rotation rates, strong absorption of certain gases, or strong magnetic fields. However, these methods are not suitable for detecting the rotation period of Earth-like exoplanets. In the foreseeable future, the most promising strategy for detecting the rotation period of an Earth-like exoplanet is to analyze the single-pixel observations of reflected starlight from the exoplanet, which can be used to retrieve surface features (Aizawa et al. 2020; Fan et al. 2019; Aizawa et al. 2020; Gu et al. 2021). Although the reflected starlight of an Earth-like exoplanet will be extremely faint compared to its star, high-contrast imaging capabilities such as a coronagraph or starshade (an external occulter in a telescope designed to suppress the light from the star; Cash 2006; Vanderbei et al. 2007) will allow us to directly image Earth-like exoplanets. For example, in an overview of the noise budget of starshade-assisted exoplanet imaging, Hu et al. (2021) showed that for some nearby stars (for example, tau Ceti and epsilon Indi A), a signal-to-noise ratio of 20 in a narrow spectral band can be achieved for an Earth-size planet in the habitable zone of its host star with an integration time of several hours using a HabEx-like telescope. The integration time would be shorter for a wider bandpass. It should therefore be feasible to detect the rotation period of Earth-like exoplanets in the near future.

In this study, we explore the detectability of the rotation period of an Earth-like exoplanet. We use the exoplanetary community atmospheric model (ExoCAM) global climate model (GCM) to simulate the atmospheric dynamics and radiative transfer for an Earth-like exoplanet with different
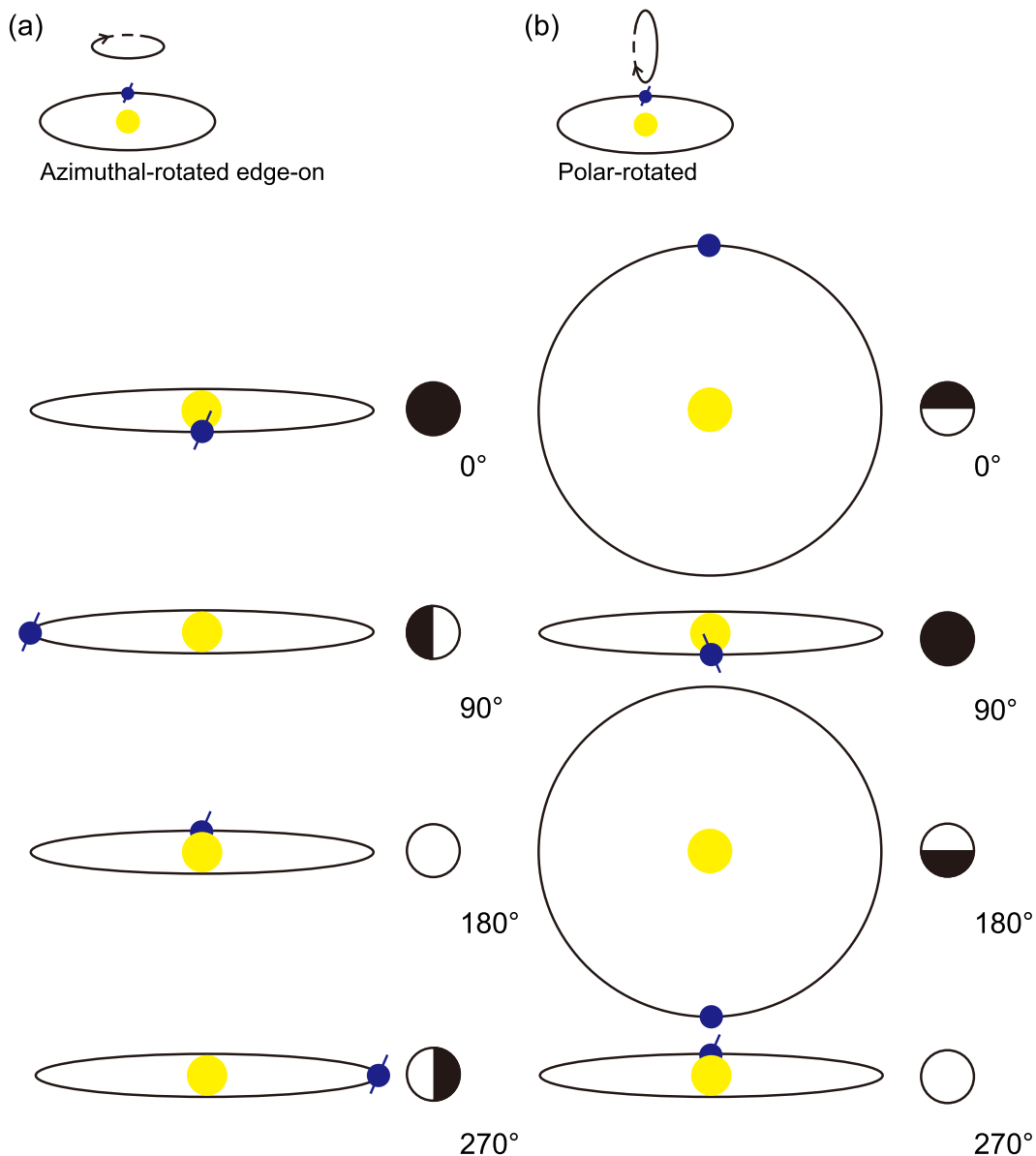
Figure 1. Two divergent sets of orbital geometries used in this study. On the top of each panel, the small diagram shows how we rotate the orbit to obtain different orbital geometries. The diagrams below show the correspondence between the angles and the orbital geometries. (a) The exoplanet is in an azimuthal-rotated edge-on orbit. (b) The exoplanet is in a polar-rotated orbit. The markers next to each diagram represent the orientation of the sunlit disk in the view of the observer.

rotation periods. Using the simulation results, we mimic future observations of an exoplanet and study which parameters of the exoplanet determine the detectability of its rotation period. We also explore the orbital geometry, wavelength, time duration, and frequency of simulated observations. We describe the ExoCAM model setup in Section 2. In Section 3, we show how we mimic exoplanet observations and obtain the rotation period from them. We investigate the influence of different parameters on the detectability of the rotation period in Section 4. We present a summary and discussion in Section 5.

2. ExoCAM GCM

We use the GCM ExoCAM (Wolf & Toon 2015; Kopparapu et al. 2016, 2017; Wolf et al. 2017; Wolf 2017) to simulate the atmosphere of Earth-like exoplanets. ExoCAM is modified from the Community Atmosphere Model version 4. It uses correlated-k radiative transfer with updated spectral coefficients using the HITRAN 2012 database and a novel treatment of water vapor continuum absorption. Crucially for this project, ExoCAM provides radiative output in 68 wavelength bins. ExoCAM calculates variable clouds as functions of time and space. We use the Rasch & Kristjánsson (1998) subgrid parameterization and the Zhang & McFarlane (1995) convection. ExoCAM has previously been used for a wide variety of studies of the atmospheric circulation and climate of terrestrial exoplanets, including cloud behavior (Wolf & Toon 2015; Kopparapu et al. 2016, 2017; Wolf et al. 2017; Wolf 2017; Haqq-Misra et al. 2018; Komacek & Abbot 2019; Yang et al. 2019a; May et al. 2021).

Since there is nothing special about Earth's rotation period (one day), we conduct two GCM experiments which are equivalent except that they have different rotation periods (one day and two days). Each simulation has an Earth-like ocean-land distribution, planetary radius, surface gravity, obliquity (23.5°), orbital eccentricity (0.0167), and orbital period. The atmosphere
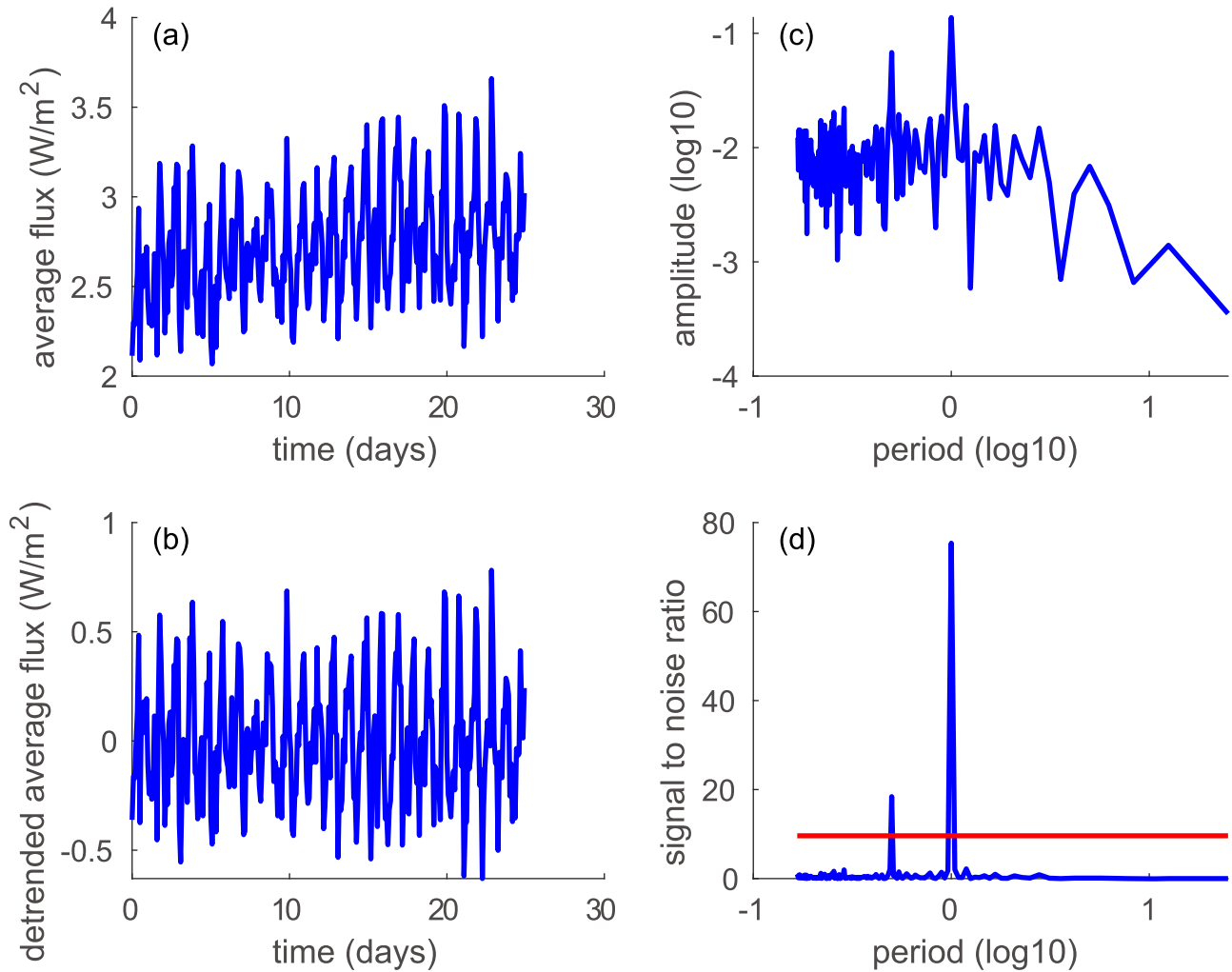
Figure 2. How we derive the rotation period from a time series. (a) A simulated time series of reflected starlight for the 1 day rotation period experiment. (b) The detrended time series. (c) Fourier transform of the detrended time series. (d) Signal-to-noise ratio as a function of period. The red line indicates the signal-to-noise threshold for 99% confidence.

is composed purely of nitrogen gas, N_2. The irradiation is equivalent to that of Earth (1360 W/m2) and the incident stellar spectrum is the same as the Sun's. The ocean is simulated with a 50 m deep slab-ocean model with thermodynamic sea ice (Bitz et al. 2012). We use a horizontal grid of $4° \times 5°$ with 40 vertical layers (Komacek & Abbot 2019). The experiments have a typical duration of approximately 15 yr with a time step of 15 minutes. We run the simulations until the annual and global-mean temperature converges, then we output two hourly-averaged radiation data over a range of wavenumbers (1 cm^{-1}–42087 cm^{-1}). In what follows, we simulate reflected starlight observations with the output from these two GCM experiments.

3. Deriving the Rotation Period from Reflected Light Time Series

We calculate the disk-averaged reflected stellar flux of the simulated exoplanet to mimic a real observation. The ExoCAM simulation provides us with the reflected stellar flux as a function of wavelength, latitude, and longitude. To calculate a time series of the disk-averaged flux, we first need to pick an orbital geometry. It should be noted that any orbital geometry is possible for an unknown exoplanet. Therefore, we use two divergent sets of orbital geometries in our analysis (Figure 1).

In the first set of orbital geometries, the orbit of the exoplanet is edge-on in the perspective of the observer (hereafter referred as azimuthal-rotated edge-on orbit). The transit configuration is defined as 0°, while the secondary eclipse configuration is defined as 180° (see Figure 1(a)). In the second set of orbital geometries (hereafter referred to as polar-rotated orbit), the orbit of the exoplanet is polarly rotated starting from a face-on orbit. The face-on orbit with the northern/southern hemisphere exposed to the observer is defined as 0°/180°, while the transit and secondary eclipse configurations are defined as 90° and 270°, respectively (see Figure 1(b)). We note that azimuthally and polarly rotating an orbit will generate all possible orbital geometries. It should also be noted that we pick the orbital geometry at the start of the time series. Because of the revolution of the planet, the immediate orbital geometry will change with time. Once an orbital geometry and a specific wavelength range are chosen, a time series of the disk-averaged reflected solar flux can be calculated from the simulation results. The original resolution of the time series is 2 hr, which is the same as the time resolution of the model output. By averaging nearby data points, the resolution of the time series can be arbitrarily decreased. We also add simulated Gaussian observational errors to the time series in order to mimic real observations.
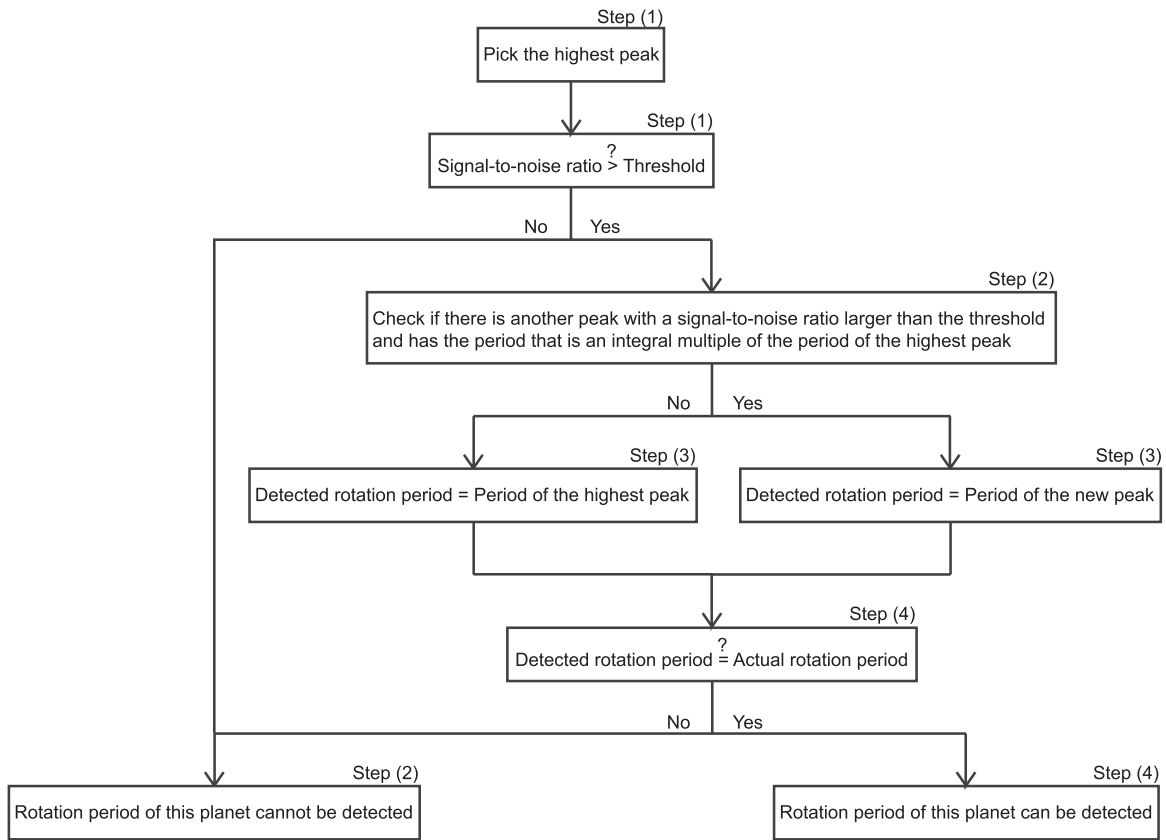
Figure 3. The flowchart of the algorithm that is used to determine whether the rotation period of the exoplanet can be detected from a simulated time series.

Figure 2(a) presents an example of a time series of simulated reflected starlight created from model output. In this case, we use the one-Earth-day rotation period simulation output in the wavelength range between 540 nm and 550 nm and the length of the time series is 25 days. The orbital geometry at $t = 0$ is set at 220° of the azimuthal-rotated edge-on orbit and the time resolution is 2 hr. The standard deviation of the observational error is set to be 5% of the disk-averaged flux, which approximately corresponds to a signal-to-noise ratio of 20 for the telescope. We also show the detrended time series, the fast Fourier transform (FFT) of the detrended time series, and the signal-to-noise ratio in Figure 2. The signal-to-noise ratio, which is the power density of the signal divided by the variance of the normally distributed observational error (Scargle 1982), is calculated from the time series (shown in Figure 2(d)). To report a signal with high confidence (low false alarm probability), the signal-to-noise ratio must exceed a certain threshold. In Figure 2(d), the red line represents the 99% confidence signal-to-noise ratio threshold calculated according to Scargle (1982). It should be noted that this threshold is a function of the length of the time series. Based on Figure 2(d), there are two signals detected with >99% confidence (<1% false alarm probability). The periods of the highest and the second highest peaks are 1.0 day and 0.5 day, respectively. The 1.0 day signal corresponds to the rotation period while the 0.5 day signal corresponds to possible periodic patterns associated with land-ocean contrast or cloud distribution. It is possible for the highest peak to occur at 0.5 day, 0.33 day or even 0.25 day rather than 1.0 day. Therefore, we propose the following algorithm to obtain the rotation period from a time series:

1. Pick the highest peak in the FFT result, then check if the signal-to-noise ratio of this peak is above the 99% confidence threshold.
2. If not, then we consider that the rotation period cannot be detected from this time series. If yes, then check if there is another peak that is above the signal-to-noise threshold and has the period that is an integral multiple of the period of the highest peak.
3. If not, the rotation period we detect is the period of the highest peak. If yes, the rotation period we detect is this integral multiple of the period of the highest peak.
4. Finally, check if the rotation period we detect is the actual rotation period of the simulated exoplanet. If yes, we consider that the rotation period can be detected from this time series.

Figure 3 contains a flowchart illustrating our algorithm. With steps (1)–(4), we can determine whether the rotation period of the exoplanet can be detected from a simulated time series. When we alter the parameters of the simulated observation (e.g., orbital geometry, wavelength range, etc.), the time series and the detectability of the rotation period change. In the next section, we will explore how different parameters influence the detectability of the rotation period of an Earth-like exoplanet.

4. Sensitivity of the Detectability of the Rotation Period to Parameters

To understand the conditions under which the rotation period of an Earth-like exoplanet is likely to be detectable, here we consider seven important factors that affect the observations.
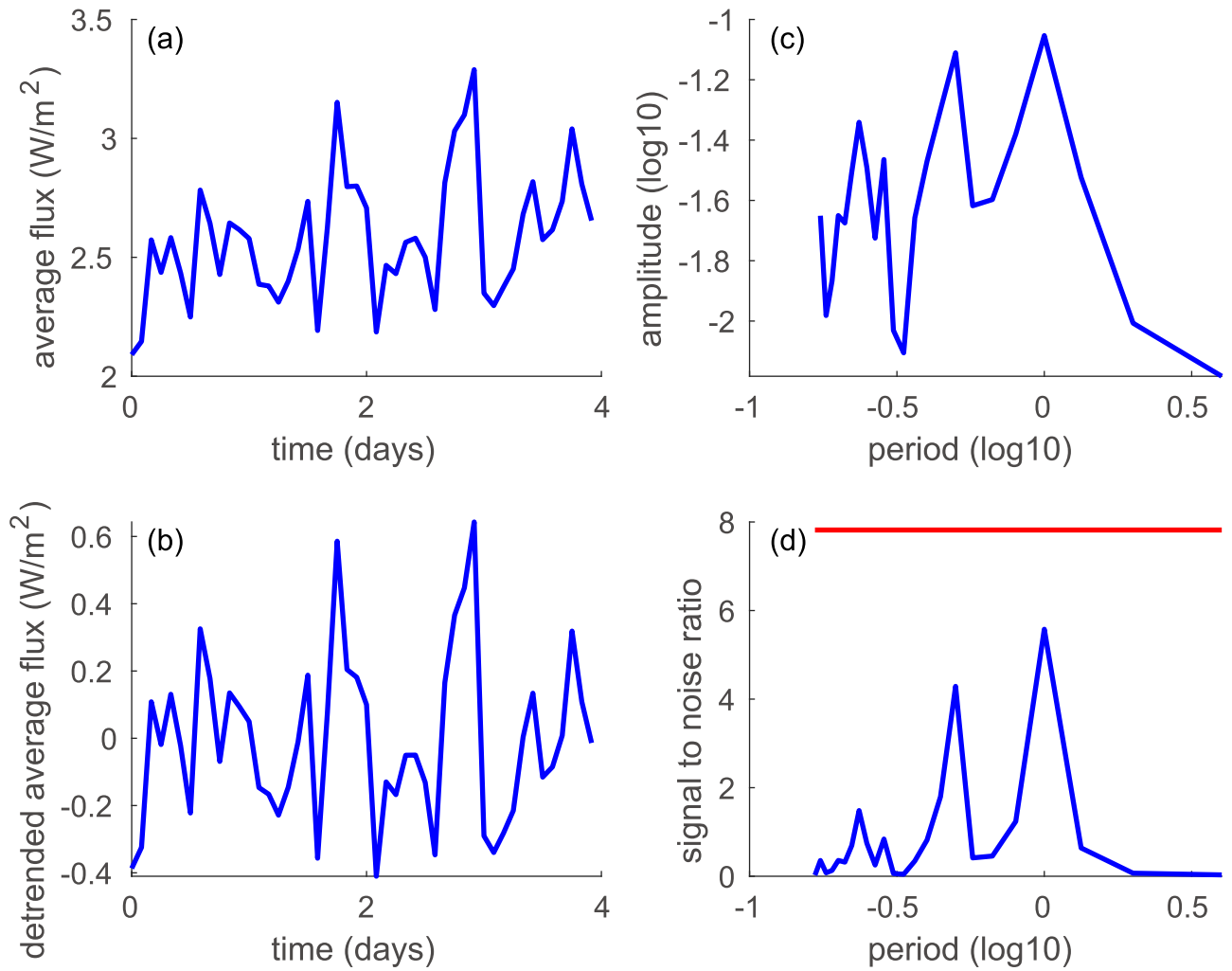
Figure 4. Same as Figure 2, except the length of the time series is 4 days. The 99% confidence threshold in panel (d) is lower than the threshold in Figure 2(d) due to the shorter time series.

4.1. Length of Observation

We find that it is generally easier to detect the rotation period with longer lengths of observation. Figure 4 shows a time series that is obtained under the same condition as the time series in Figure 2 except that the length of this time series is only 4 days. From Figure 4(d), we clearly see that this time series does not meet our criteria for rotation period detection. Therefore, under a given condition, the minimum length of observation needed to detect the real rotation period is a key parameter that measures the detectability of the rotation period.
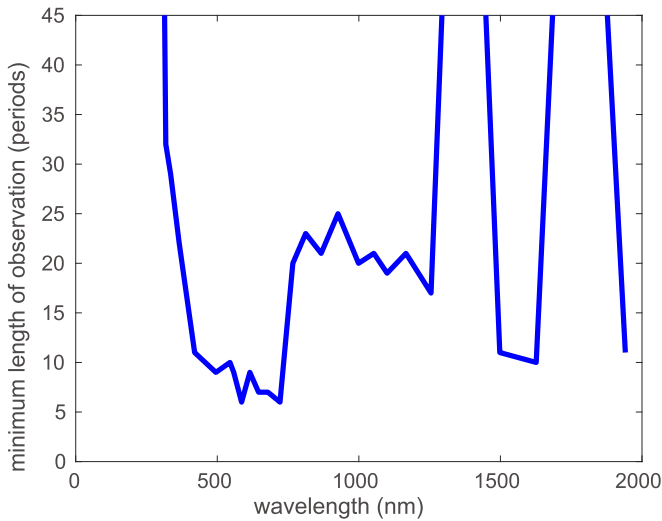
4.2. Rotation Period

Since the detectability of the rotation period depends on how many periods are contained in the time series, the minimum length of observation needed to detect the rotation period should be measured in periods instead of days. In Section 3, we used one per 2 hr, one per 4 hr, etc., to represent the time resolution of the time series. Since hour and day are Earth-specific units, a more sophisticated way to describe the time resolution is the number of data points in one period. In other words, one per 2 hr for a 1 day rotation period and one per 4 hr for a 2 day rotation period data set are equivalent, each corresponding to 12 data points per period. Ideally the minimum observation length

needed to detect the rotation period should be a constant number of rotational periods. However, our analysis shows that sometimes the minimum length of observation (in rotational periods) needed for the 1 day rotation period data set and the minimum length of observation needed for the 2 day rotation period data set are not always equal due to the differing climates. In what follows we will regard the minimum length of observation needed to detect the rotation period under a given condition as the larger minimum length of observation obtained from the two data sets.

4.3. Wavelength

The detectability of the rotation period may vary with the wavelength used to observe the exoplanet. Here we fix the orbital geometry at $180°$ of the azimuthal-rotated edge-on orbit, the time resolution at 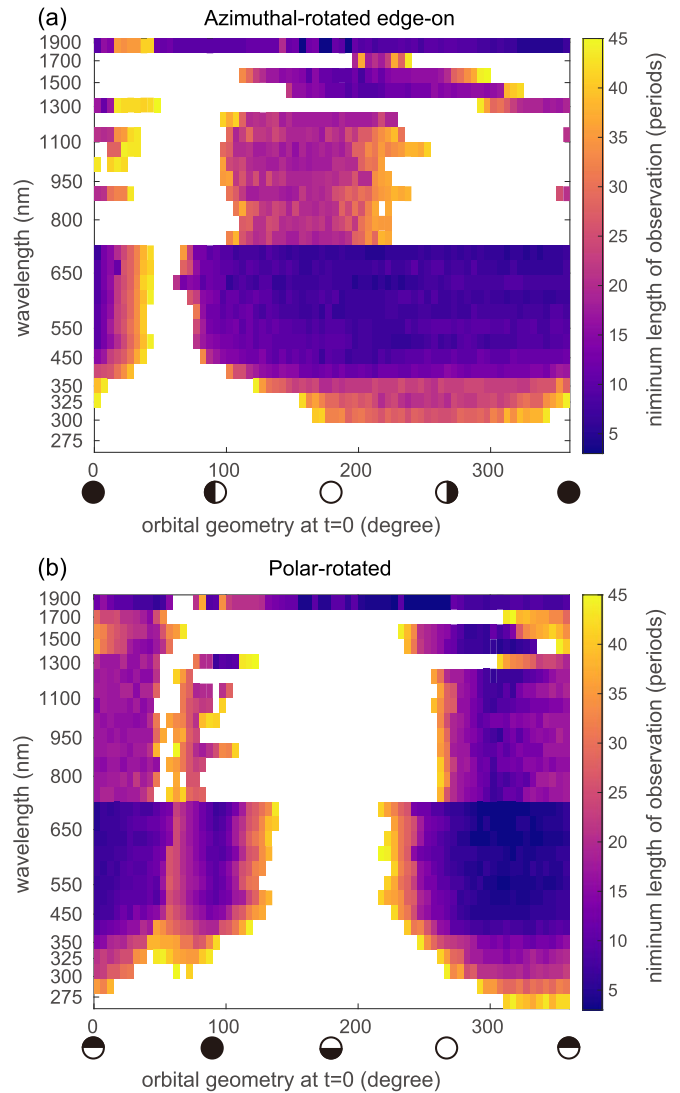12 data points per period and the observational error at 5%. We then calculate the minimum length of observation needed to detect the rotation period for different wavelength ranges (Figure 5.) If the rotation period cannot be obtained from an observational length of 45 rotation periods, we consider the rotation period to not be detectable under this condition. In Figure 5, we can see that the minimum length of observation needed in the visible channels (500 to

Figure 5. An example of the minimum length of observation needed to detect the rotation period as a function of wavelength. We combine 1 and 2 day period data here (see Section 4.2) and use a 99% confidence threshold. The orbital geometry is 180° of the azimuthal-rotated edge-on orbit, the time resolution 12 data points per period, and the observational error is 5%.

700 nm) is less than 10 periods, much shorter than the minimum length of observation needed for the ultraviolet and near-infrared channels. This is mainly because the reflectance of land, ocean, and cloud are more diverse in the visible channels than in other channels (Xu et al. 2015; Kokaly et al. 2017).

4.4. Orbital Geometries

If the exoplanet is near secondary eclipse, the observer can see almost the entire sunlit disk (as long as the star is not blocking the planet), which will provide a smooth variation in reflected light. If the exoplanet is near transit, the observer can see very little reflected starlight from the exoplanet, which will make the variation in reflected light rather random. Therefore, the orbital geometry clearly influences the detectability of the rotation period. In the following, we fix the time resolution at 12 data points per period and the observational error at 5%, then find the minimum length of observation needed to detect the rotation period as a function of wavelength and orbital geometry (shown in Figure 6). For the near-infrared channels below 1.3 μm, in a range of ~100° in both azimuthal and polar angle around the secondary eclipse, the rotation period is detectable with ~20–30 periods of observation. In the visible channels, the rotation period is detectable with less than 15 periods of observation in a much larger geometry range. As expected, the rotation period of the exoplanet is only difficult to detect near transit. For the ultraviolet channels with wavelengths above 285 nm, the rotation period is detectable near the secondary eclipse with more than 25 periods of observation. The rotation period is undetectable at wavelengths less than 285 nm. In Figure 6(a), we can see that the most detectable/undetectable orbital geometries are not exactly at secondary eclipse/transit. That is because the orbital geometry is picked at $t = 0$ and will change due to the revolution of the planet.

4.5. Time Resolution

To evaluate the influence of time resolution on the detectability of the rotation period, we repeat the analysis from Section 4.4 with coarser time resolutions of six data points per period


Figure 6. The minimum length of observation needed to detect the rotation period as functions of the wavelength and orbital geometry. We combine 1 and 2 day period data here (see Section 4.2) and use a 99% confidence threshold. The time resolution is 12 data points per period. The observational error is 5%. (a) Azimuthal-rotated edge-on orbital geometries (see Figure 1). (b) Polar-rotated orbital geometries. The color white indicates that the rotation period is not detectable.

(Figure 7(a)), four data points per period (Figure 7(b)), and three data points per period (Figure 7(c)). With six data points per period, the rotation period is still detectable in a large geometry range in visible channels, but the minimum length of observation needed to detect the rotation period becomes about two times longer than the higher resolution scenario (Figure 7(a)). In contrast, the rotation period becomes undetectable at other wavelengths. If the time resolution is decreased to three data points per period, the rotation period is only detectable near transit (Figure 7(c)). This is consistent with Jiang et al. (2018), who showed that when the time resolution is lower than two data points per period, the probability of detecting the rotation period drops dramatically regardless the total observation length.
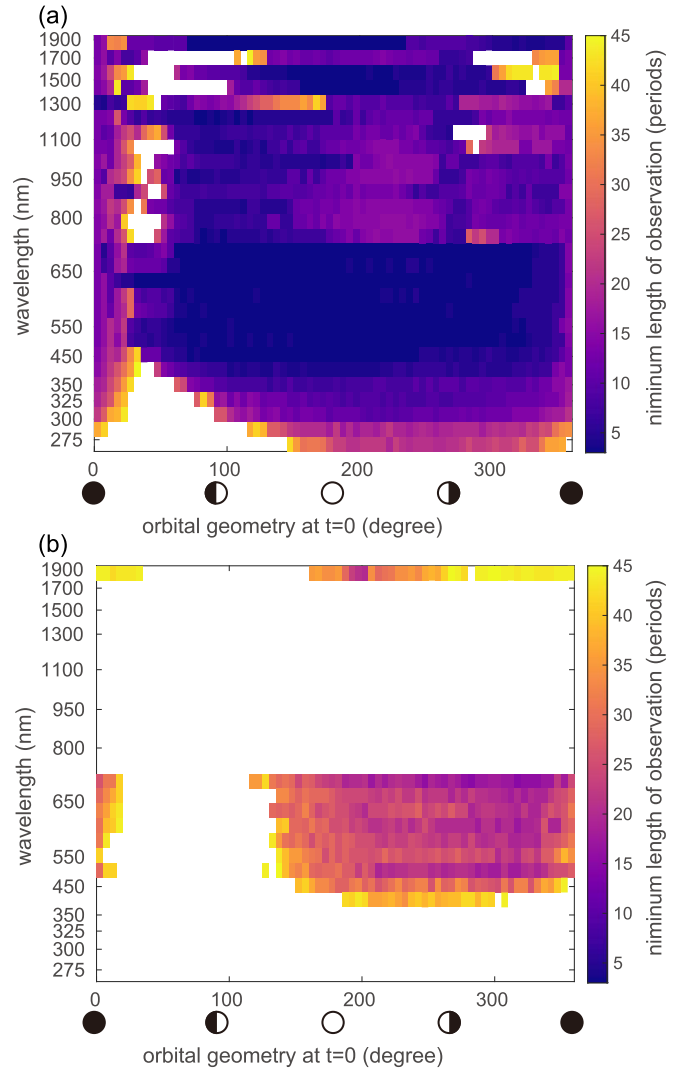
4.6. Observational Error

In the previous analysis, we fixed the standard deviation of the observational error added to the time series at 5% of the
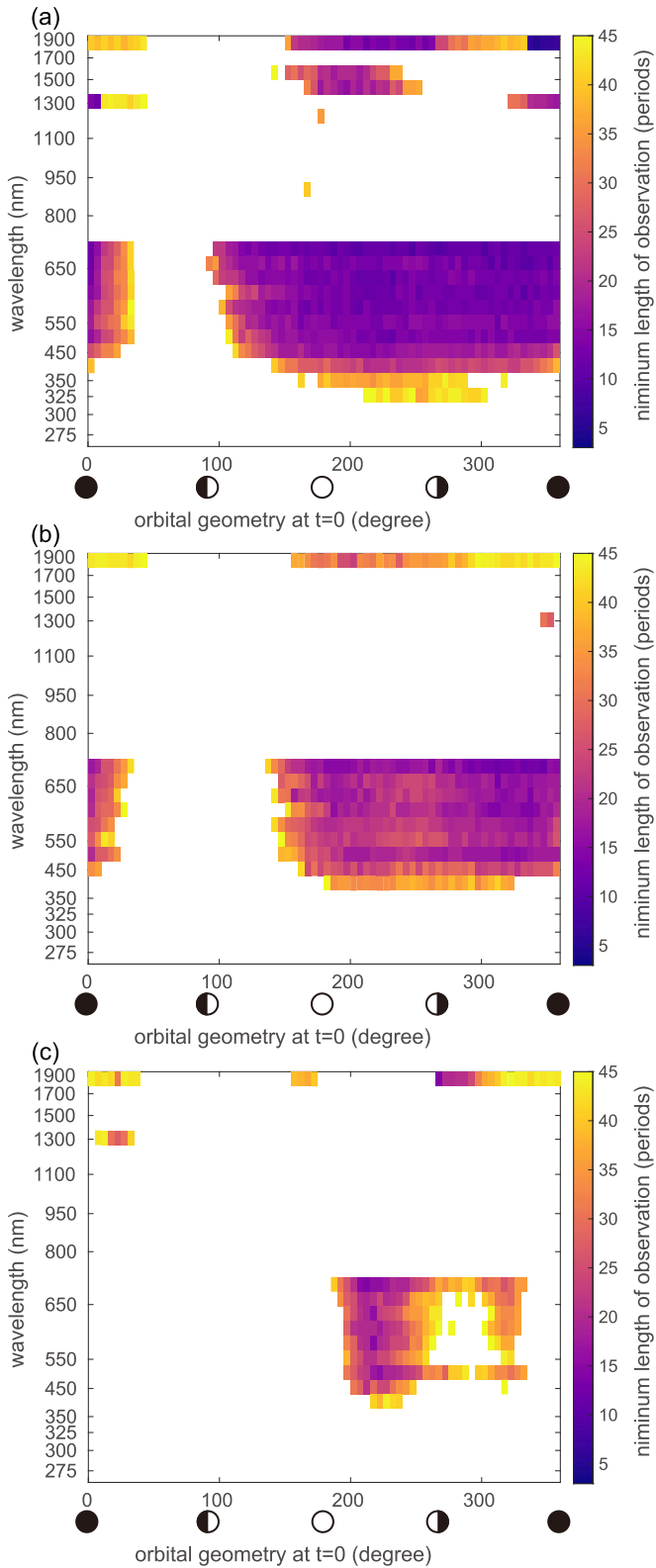
Figure 7. (a) Same as Figure 6(a), except that the time resolution is six data points per period. (b) Same as Figure 6(a), except that the time resolution is four data points per period. (c) Same as Figure 6(a), except that the time resolution is three data points per period.

Figure 8. (a) Same as Figure 6(a), except that the S/N is 40. (b) Same as Figure 6(a), except that the S/N is 10.

change the S/N to 40 and 10 (Figure 8). When the S/N is 40, the detectability is significantly enhanced in all channels (Figure 8(a)). In the visible and near-infrared channels, the minimum length of observation needed to detect the rotation period is less than 10 periods for most of the orbital geometries. Moreover, even the ultraviolet channels at wavelengths below 285 nm become detectable. On the contrary, when the S/N is 10 (Figure 8(b)), the rotation period is undetectable for most of the ultraviolet and near-infrared channels. Although the rotation period is still detectable for the visible channels, it requires more than 20–25 periods of observation.

4.7. Land Fraction

The fractions of land and ocean on Earth's northern hemisphere are comparable, whereas on Earth's southern hemisphere the ocean covers more than 80% of the surface. Therefore, the southern hemisphere of the Earth is more like an aqua planet (i.e., a planet with full ocean coverage). We can exploit this asymmetry to investigate how land fraction influences the detectability of the rotation period. For example, when the observer focuses on the northern hemisphere (around 0° of the second set of orbital geometries), the

disk-averaged flux, which approximately corresponds to a signal-to-noise ratio (S/N) of 20 for each integration. To evaluate the influence of the S/N on the detectability of the rotation period, we recreate our analysis from Section 4.4 but

rotation period is detectable for most of the channels (Figure 6(b)). In contrast, when the observer focuses on the southern hemisphere (around 180° of the second set of orbital geometries), the rotation period becomes undetectable. This result implies that the rotation period of an exoplanet with no land is unlikely to be detected using the observational technique outlined here. In other words, an exoplanet whose rotation period can be detected is likely to have a mix of continents and ocean, which may be used to infer information about the planet's geophysical and geochemical context that would otherwise be hidden.

5. Conclusion and Discussion

In this study, we simulate observations of ExoCAM output, a GCM that includes clouds, to evaluate the detectability of a terrestrial exoplanet's rotation period through an FFT analysis of reflected starlight. Our work shows that to better detect the rotation period, one needs to plan the observation so that each individual integration would yield a $S/N > 10$, while keeping the integration time shorter than $1/6$–$1/4$ of the rotation period of the planet. The best wavelength range to carry out this observation will be between 500 and 700 nm, and in this wavelength range, the rotation period may be obtained with an observation campaign that lasts for $\sim$10 rotation periods. Using Earth as an analog, the quantities above correspond to repeating the integration every $<$4–6 hr for $\sim$10 days. There are trade-offs between the integration time (and thus the S/N per integration) and the total duration of the observation. The optimal timing of this type of observation will be when the planet moves into an orbital phase where much of the planetary surface is illuminated by starlight.

When dealing with a real observation, since we would not know the rotation period, one should follow the steps in Section 3 to get a preliminary rotation period from the observed time series. With the preliminary rotation period, the observer will be able to convert the time resolution to units of number per period and the length of the time series to a multiple of the rotation periods. By comparing the parameters of the observation (time resolution, S/N, length of observation, etc.) to the parameter space explored in Section 4, one can tell whether this preliminary rotation period is likely to be the true rotation period or not.

Future space telescopes being planned may provide the required conditions to detect the rotation periods of terrestrial planets in the habitable zone of some nearby stars. For example, a HabEx-like telescope would achieve an $S/N = 20$ per 5 nm spectral channel in 500–700 nm for an Earth-like planet in the habitable zone of the nearest stars (distance $<$4 pc, e.g., tau Ceti, epsilon Indi A) in $\sim$10 hr (Hu et al. 2021). This translates to an integration time of $\sim$6 hr per $\sim$10 nm spectral channel, corresponding to the simulation shown in this paper. The rotation period would thus be detectable if Earth analogs are found in these systems and $\sim$10 days of the mission time are dedicated to the campaign. Given the importance of the rotation period (it is one of the basic planetary parameters aside from mass and radius) and possible science that can be achieved at the same time (e.g., surface composition mapping; Cowan et al. 2009; Fan et al. 2019), a $\sim$10 day campaign may be favorable. The requirement will be less stringent for planets larger than Earth or closer to their host star, for which the endeavor of detecting the planetary rotation period may be extended to stars further away. A larger space telescope (e.g., the LUVOIR mission concept) would enable rotation period detection in more systems.

The detectability of rotation period is mainly due to the differences between the reflectance of ocean, land, and persistent cloud. In general, clouds block land and ocean from the observer, making the rotation period more difficult to detect. In a test run, we removed the cloud from the simulated planet and found that the minimum length of observation needed to detect the rotation period was shorter than it was for the cloud-covered planet. While the impact of clouds is essential, the modeling of clouds is highly uncertain (Yang et al. 2019b). Future work exploring alternative cloud schemes is needed. For Earth-like exoplanets, since the planet is not entirely covered by cloud, its surface features can be seen by the observer so that the rotation period is detectable. For exoplanets with more substantial cloud coverage than Earth, the rotation period may become undetectable. For example, Lee et al. (2020) found that a periodogram analysis of the light curve of Venus reveals two strong signals at 3.7 and 4.6 days, which correspond to the rotation of the atmosphere rather than the rotation of Venus itself.

In Section 4.7, we proposed that the rotation period of an aqua exoplanet is likely undetectable. However, this is based on the precondition that we only have photometric observations of the exoplanet. Ocean glint, which has been shown to facilitate surface mapping of potential habitable exoplanets (Lustig-Yaeger et al. 2018), is highly polarized. Kopparla et al. (2018) model the polarization signal of the TRAPPIST-1 system and show that the polarization signal from an ocean-covered exoplanet is stronger and easier to detect than the intensity signal. Since the polarization observation of an aqua exoplanet is dependent on the surface roughness of the ocean, a nonuniform surface roughness distribution of the aqua exoplanet could cause diurnal variation in a polarization observation. If a direct-imaged polarization observation of an exoplanet were available, the rotation period of an aqua exoplanet might still be detectable. In concert with photometric observations, a polarization observation may also improve the detectability of the rotation period of Earth-like exoplanets.

In this paper, we have studied fast-rotating exoplanets, whose rotation period is much smaller than its orbital period. For Venus-like, slowly-rotating exoplanets whose rotation period is comparable to their orbital period, the variation of the reflected starlight caused by its rotation would be coupled with the variation caused by its revolution so that the signal of the rotation period may be hard to detect. Further studies are required to address this problem.

In summary, we find that it will be possible to detect the rotation period of a terrestrial exoplanet using direct imaging if the planet is observed in favorable conditions. The detection of the rotation period of Earth-like exoplanets will help us identify habitable exoplanets and provide us with information on the dynamical evolution of exoplanetary systems.

Data Statement

The ExoCAM model source code and related data are available to download from https://github.com/storyofthewolf/ExoCAM. The computed data underlying this article are described in the article. For additional questions regarding the data and code sharing, please contact the corresponding author.

ORCID iDs

Jiazheng Li ⓘ https://orcid.org/0000-0002-2563-6289
Jonathan H. Jiang ⓘ https://orcid.org/0000-0002-5929-8951
Huanzhou Yang ⓘ https://orcid.org/0000-0001-8693-7053
Dorian S. Abbot ⓘ https://orcid.org/0000-0001-8335-6560
Renyu Hu ⓘ https://orcid.org/0000-0003-2215-8485
Thaddeus D. Komacek ⓘ https://orcid.org/0000-0002-9258-5311
Stuart J. Bartlett ⓘ https://orcid.org/0000-0001-5680-476X
Yuk L. Yung ⓘ https://orcid.org/0000-0002-4263-2562

References

Aizawa, M., Kawahara, H., & Fan, S. 2020, ApJ, 896, 22
Barnes, R. 2017, CeMDA, 129, 509
Bitz, C. M., Shell, K. M., Gent, P. R., et al. 2012, JCli, 25, 3053
Brogi, M., De Kok, R. J., Albrecht, S., et al. 2016, ApJ, 817, 106
Cash, W. 2006, Natur, 442, 51
Cowan, N. B., Agol, E., Meadows, V. S., et al. 2009, ApJ, 700, 915
Fan, S., Li, C., Li, J. Z., et al. 2019, ApJL, 882, L1
Forget, F., & Leconte, J. 2014, RSPTA, 372, 20130084
Gu, L., Fan, S., Li, J., et al. 2021, AJ, 161, 122
Haqq-Misra, J., Wolf, E. T., Joshi, M., et al. 2018, ApJ, 852, 67
Hess, S. L. G., & Zarka, P. 2011, A&A, 531, A29
Hu, R., Lisman, D., Shaklan, S., et al. 2021, JATIS, 7, 021205
Jiang, J. H., Zhai, A. J., Herman, J., et al. 2018, AJ, 156, 26
Kaspi, Y., & Showman, A. P. 2015, ApJ, 804, 60
Kasting, J. F., Whitmire, D. P., & Reynolds, R. T. 1993, Icar, 101, 108
Kokaly, R. F., Clark, R. N., Swayze, G. A., et al. 2017, US Geological Survey Data Release, Usgs Spectral Library v7, United States Geological Survey (USGS), Reston, VA
Komacek, T. D., & Abbot, D. S. 2019, ApJ, 871, 245
Kopparapu, R. K., Wolf, E. T., Arney, G., et al. 2017, ApJ, 845, 5
Kopparapu, R. K., Wolf, E. T., Haqq-Misra, J., et al. 2016, ApJ, 819, 84
Kopparla, P., Natraj, V., Crisp, D., et al. 2018, AJ, 156, 143
Lee, Y. J., Muñoz, A. G., Imamura, T., et al. 2020, NatCo, 11, 1
Lustig-Yaeger, J., Meadows, V. S., Mendoza, G. T., et al. 2018, AJ, 156, 301
May, E. M., Taylor, J., Komacek, T. D., et al. 2021, ApJL, 911, L30
Rasch, P. J., & Kristjánsson, J. E. 1998, JCli, 11, 1587
Scargle, J. D. 1982, ApJ, 263, 835
Showman, A. P., Wordsworth, R. D., Merlis, T. M., et al. 2013, in Comparative Climatology of Terrestrial Planets, ed. S. J. Mackwell et al. (Tucson, AZ: Univ. of Arizona Press), 277
Snellen, I. A., Brandl, B. R., de Kok, R. J., et al. 2014, Natur, 509, 63
Vanderbei, R. J., Cady, E., & Kasdin, N. J. 2007, ApJ, 665, 794
Way, M. J., Del Genio, A. D., Kiang, N. Y., et al. 2016, GeoRL, 43, 8376
Wolf, E. T. 2017, ApJL, 839, L1
Wolf, E. T., Shields, A. L., Kopparapu, R. K., et al. 2017, ApJ, 837, 107
Wolf, E. T., & Toon, O. B. 2015, JGRD, 120, 5775
Xu, M., Pickering, M., Plaza, A. J., et al. 2015, ITGRS, 54, 1659
Yang, J., Abbot, D. S., Koll, D. D., et al. 2019a, ApJ, 871, 29
Yang, J., Boué, G., Fabrycky, D. C., et al. 2014, ApJL, 787, L2
Yang, J., Leconte, J., Wolf, E. T., et al. 2019b, ApJ, 875, 46
Zhang, G. J., & McFarlane, N. A. 1995, JGRD, 100, 1417